HAL open science

Arsenic-Doped SnSe Thin Films Prepared by Pulsed Laser Deposition

Lubomir Prokes, Magdalena Gorylova, Katerina Cermak Sraitrova, Virginie Nazabal, Josef Havel, Petr Nemec

To cite this version:

Lubomir Prokes, Magdalena Gorylova, Katerina Cermak Sraitrova, Virginie Nazabal, Josef Havel, et al.. Arsenic-Doped SnSe Thin Films Prepared by Pulsed Laser Deposition. ACS Omega, 2021, 6 (27), pp.17483-17491. 10.1021/acsomega.1c01892 . hal-03331011

HAL Id: hal-03331011

https://hal.science/hal-03331011v1

Submitted on 22 Nov 2021

HAL is a multi-disciplinary open access archive for the deposit and dissemination of scientific research documents, whether they are published or not. The documents may come from teaching and research institutions in France or abroad, or from public or private research centers.

L'archive ouverte pluridisciplinaire **HAL**, est destinée au dépôt et à la diffusion de documents scientifiques de niveau recherche, publiés ou non, émanant des établissements d'enseignement et de recherche français ou étrangers, des laboratoires publics ou privés.

Distributed under a Creative Commons Attribution - NonCommercial - NoDerivatives 4.0 International License

ACS OMEGA

http://pubs.acs.org/journal/acsodf

Article

Arsenic-Doped SnSe Thin Films Prepared by Pulsed Laser Deposition

Lubomír Prokeš, Magdaléna Gorylová, Kateřina Čermák Šraitrová, Virginie Nazabal, Josef Havel, and Petr Němec*

Cite This: *ACS Omega* 2021, 6, 17483−17491

Read Online

ACCESS | Metrics & More | Article Recommendations

ABSTRACT: Pulsed UV laser deposition was exploited for the preparation of thin $Sn_{50-x}As_xSe_{50}$ (x = 0, 0.05, 0.5, and 2.5) films with the aim of investigating the influence of low arsenic concentration on the properties of the deposited layers. It was found that the selected deposition method results in growth of a highly (h00) oriented orthorhombic SnSe phase. The thin films were characterized by different techniques such as X-ray diffraction, scanning electron microscopy with energy-dispersive X-ray spectroscopy, atomic force microscopy, Raman scattering spectroscopy, and spectroscopic ellipsometry. From the results, it can be concluded that thin films containing 0.5 atom % of As exhibited extreme values regarding crystallite size, unit cell volume, or refractive index that significantly differ from those of other samples. Laser ablation with quadrupole ion trap time-of-flight mass spectrometry was used to identify and compare species present in the plasma originating from the interaction of a laser pulse with solid-state $Sn_{50-x}As_xSe_{50}$ materials in both forms, i.e. parent powders as well as deposited thin films. The mass spectra of both materials were similar; particularly, signals of $Sn_mSe_n^+$ clusters with low m and n values were observed.

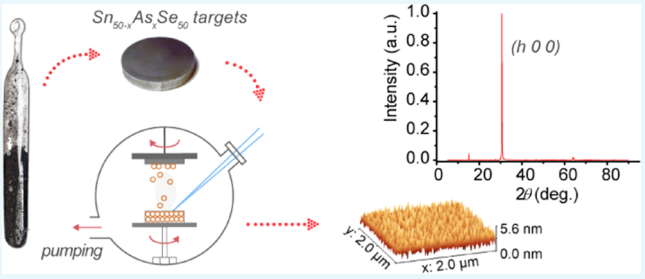

1. INTRODUCTION

Because of their two-dimensional (2D) character, tin selenides are studied as prospective anode materials for ion batteries[1] and capacitors for energy storage.[2] Tin selenide (SnSe)[3,4] and its composites with graphene oxide[5] are perspective materials for electronics, optoelectronics, and solar cells[6] and also analytical voltammetry.[7] Moreover, SnSe has interesting thermoelectric properties in terms of low thermal conductivity and high thermoelectric figure of merit.[8,9] Tin forms basically two selenides—SnSe and $SnSe_2$.[10,11] Another Sn−Se compound with stoichiometry Sn_3Se_4 is stable only at high pressures (18−70 GPa).[12]

Tin diselenide ($SnSe_2$) is a material suitable for infrared[13] and ultraviolet[14] photodetection, photocatalysis,[15] surface-enhanced Raman scattering (SERS) spectrometry,[16] and as sensors for gases[17] or ammonia ions.[18] Tin selenides of different stoichiometry (SnSe, $SnSe_2$, and Sn_2Se_3) were also investigated for their potential phase-change memory applications.[19]

To improve the properties of SnSe, many elements or compounds have been studied as potential dopants, such as Ag,[20] Zn,[21] Cu,[22] etc. for p-type doping and Bi[23] for n-type doping. To influence the formation and concentration of native defects in SnSe (i.e., Sn and/or Se vacancies or Se interstitials), another strategy employing doping with elements of ambivalent nature could be used. It has been shown that one of such doping elements could be arsenic, which was recently studied as a dopant for single-crystalline SnSe materials.[24] Importantly, the authors report a profound increase in concentration of tin vacancies and formation of a cluster of divacancies, which is believed to be an essential attribute of effective phase-change memory materials.[25] Moreover, they observed an unprecedented 2-orders-of-magnitude decrease in free carrier concentration induced by As-doping.[24] However, for applications in the field of phase-change memory materials, it is required to fabricate tin selenides in the form of thin films. For Sn−Se thin-film deposition, different techniques have been already studied, such as sputtering,[26] evaporation,[27] spray pyrolysis,[28] atomic layer deposition,[29] molecular beam epitaxy,[19] pulsed laser deposition (PLD),[30] etc. Among them and according to the material being deposited, PLD is of large interest due to its flexibility, undemanding control of the deposition process, ability to prepare multilayered structures, and often stoichiometric material transfer from the target to the films.[31,32] More specifically, the other advantages of UV

Received: April 9, 2021
Accepted: June 17, 2021
Published: June 30, 2021

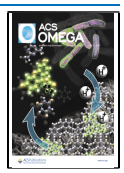

Downloaded via 86.215.150.249 on November 22, 2021 at 19:18:31 (UTC).
See https://pubs.acs.org/sharingguidelines for options on how to legitimately share published articles.

ACS Publications

© 2021 The Authors. Published by American Chemical Society

https://doi.org/10.1021/acsomega.1c01892
ACS Omega 2021, 6, 17483−17491

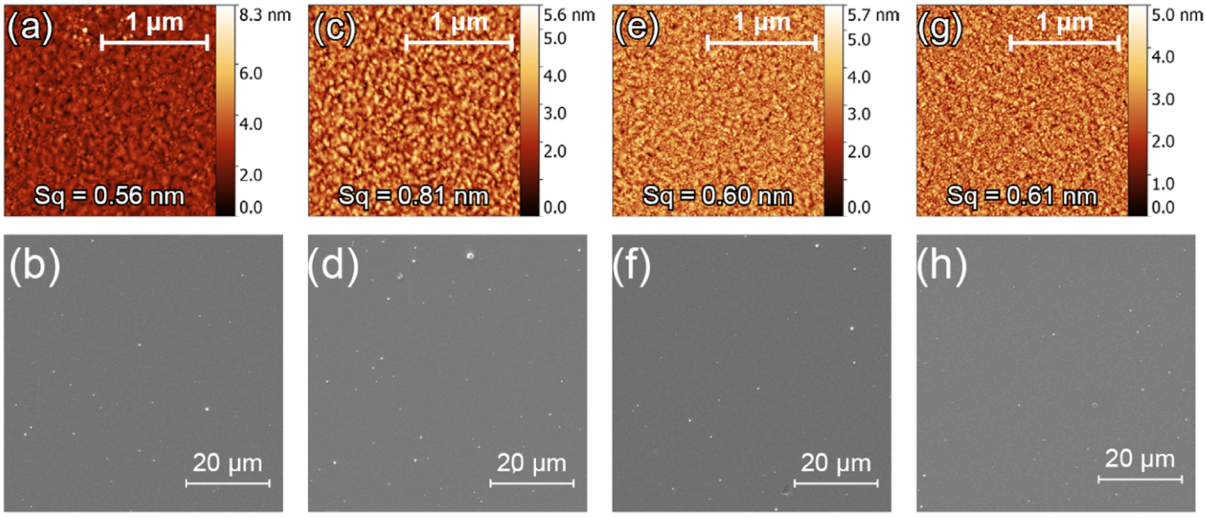

Figure 1. AFM images (2 μm × 2 μm) with root-mean-square roughness values (upper row) and SEM micrographs (bottom row) of PLD thin films: (a, b) $Sn_{47.5}As_{2.5}Se_{50}$; (c, d) $Sn_{49.5}As_{0.5}Se_{50}$; (e, f) $Sn_{49.95}As_{0.05}Se_{50}$; and (g, h) $Sn_{50}Se_{50}$.

PLD are represented by the large absorption of UV light in many materials leading to small penetration depth and by the flat-top energy distribution of the excimer laser beams (typically used for UV PLD), which causes a homogeneous energy density distribution in the ablated area. It is worth to mention that other thermoelectric thin films such as Ag-modified PbTe were deposited by PLD.[33]

Based on the information summarized above, SnSe thin layers doped with arsenic were prepared by pulsed laser deposition in this work to study the effect of doping on the properties of the films. The thin films were characterized in terms of their structure, chemical composition, morphology, topography, electrical, vibrational, and optical properties. Attention was paid to the mass spectrometry study of the species formed via interaction of UV laser pulses with the films and related powdered precursors as laser ablation with quadrupole ion trap time-of-flight mass spectrometry (QIT-TOFMS) has already been shown to be an important and powerful methodology to study the formation of clusters originating from solid-state materials.[34−37] The results of QIT-TOFMS may help us understand the processes involved in the plasma plume during pulsed laser deposition with implications for related thin-film growth and the structure of deposited layers.

2. RESULTS AND DISCUSSION

The chemical composition of prepared thin films as determined via energy-dispersive X-ray spectroscopy (EDS) in terms of tin and selenium content corresponds very well with the nominal composition of the used $Sn_{50-x}As_xSe_{50}$ (x = 0, 0.05, 0.5 and 2.5) targets: at maximum, the differences are ∼1.5 and 2.2 atom % of Sn and Se, respectively. The quantitative determination of As by EDS is problematic due to its low content; however, qualitatively arsenic was clearly identified. It is important to note that the error limit of the used EDS method is ±1 atom %.

The thin layers' morphology investigated by scanning electron microscopy (SEM) showed a smooth surface of the films (Figure 1). The presence of cracks or holes was not identified. A few (sub)micrometer-sized droplets are seen in SEM images, which is a common phenomenon for the PLD technique. The good quality of the deposited films is also evidenced by the atomic force microscopy (AFM) scans (Figure 1). For all deposited thin films, root-mean-square roughness values (S_q) determined by AFM were found to be lower than ∼0.8 nm, confirming the relatively smooth surface of the layers. The preliminary temperature-dependent electrical resistance measurements showed that all samples except the one doped with 2.5 atom % of As exhibited a resistance drop of 3−4 orders of magnitude upon heating up to 400 °C. However, we observed some peculiar features for all samples, which require a further detailed study.

X-ray diffraction (XRD) measurements of the thin films deposited on glass substrates revealed that all of the layers are crystalline—as documented in Figure 2, the XRD patterns clearly show peaks indexed to the (200), (400), (600), and (800) planes, indicating the highly (h00) oriented orthorhombic SnSe phase. We note that no signal from the substrate was detected in XRD data.

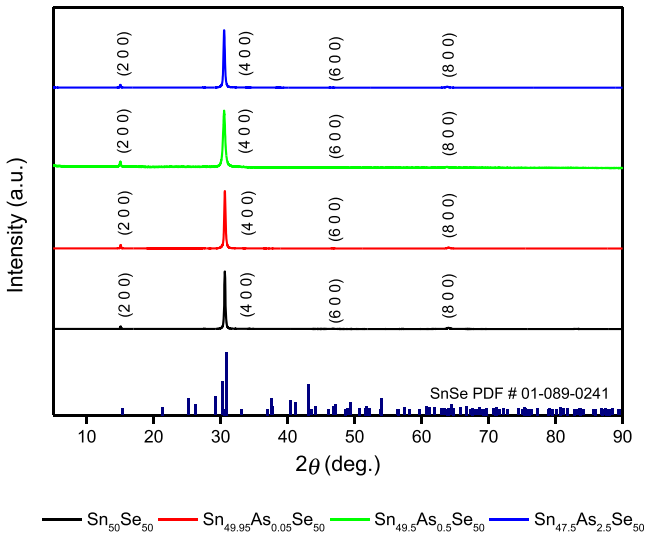

Figure 2. XRD patterns of PLD $Sn_{50-x}As_xSe_{50}$ (x = 0, 0.05, 0.5, and 2.5) thin films deposited on glass substrates. Vertical lines in the bottom panel indicate the orthorhombic SnSe as a reference (PDF # 01-089-0241 card).

https://doi.org/10.1021/acsomega.1c01892
ACS Omega 2021, 6, 17483−17491

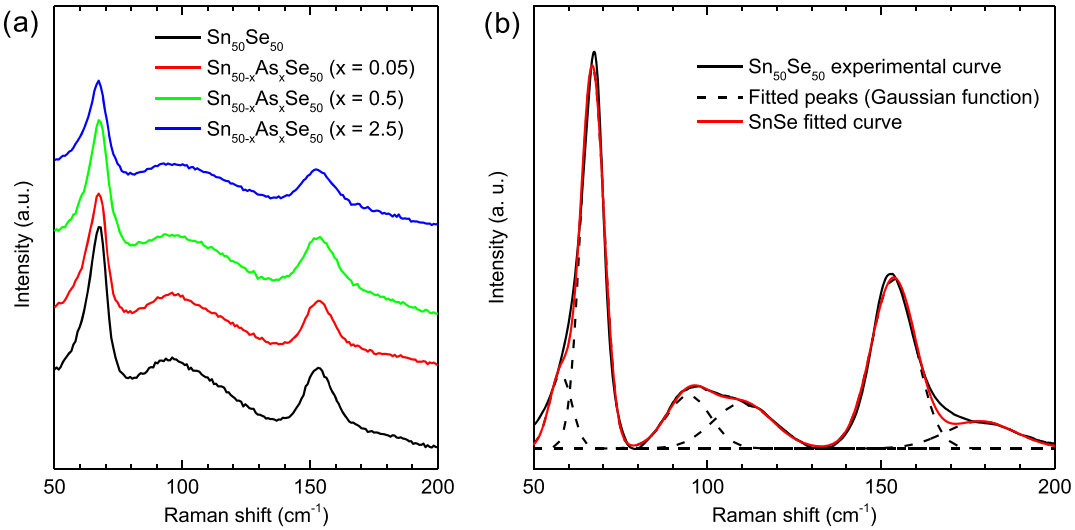

Figure 3. (a) Raman scattering spectra of PLD $Sn_{50-x}As_xSe_{50}$ (x = 0, 0.05, 0.5, and 2.5) thin films; (b) decomposition of the Raman spectrum of $Sn_{50}Se_{50}$ thin film using six Gaussians (the baseline was subtracted).

Table 1. Characteristics of $Sn_{50-x}As_xSe_{50}$ (x = 0, 0.05, 0.5, and 2.5) Thin Films Prepared by PLD Determined via Ellipsometry[a]

thin film $Sn_{50-x}As_xSe_{50}$	d (nm)	surface roughness (nm)	E_g (eV)	E_u (eV)	n@400 nm	n@1550 nm
x = 0	182	3.5	0.90	0.28	3.42	4.91
x = 0.05	181	3.8	0.90	0.29	3.51	4.85
x = 0.5	167	4.3	0.96	0.23	3.63	4.77
x = 2.5	166	4.2	0.96	0.22	3.26	4.90

[a]Thickness d (±2 nm), surface roughness (±0.2 nm), band gap E_g (±0.04 eV), Urbach energy E_u (±0.01 eV), and refractive index n at both 400 and 1550 nm (±0.01).

It was found that the crystallite size and full width at half-maximum (FWHM) of dominant XRD peaks depend on the arsenic concentration but do not vary linearly with the increasing content of arsenic. In fact, the crystallite size is within the range of ∼58−68 nm with a minimum of ∼39 nm for thin films containing 0.5 atom % of As. Consequently, FWHM varied within the range of ∼0.14−0.12° but exhibited a maximum of ∼0.21°, which was again identified for films with 0.5 atom % of As. The unit cell volume is influenced by the arsenic content too. Whereas the changes in a and c lattice parameters are within the experimental error, the b parameter shows a minimum for the layer containing 0.5 atom % of As. Due to this minimum value, the unit cell volume presents also a minimum for the same content of dopant. We note that these extreme values of parameters for 0.5 atom % of As sample coincide with the highest concentration of vacancies in SnSe single crystals doped with As.[24]

Raman scattering spectra of fabricated $Sn_{50-x}As_xSe_{50}$ thin films (measured from 50 cm^{-1}) are presented in Figure 3a. The decomposition of the Raman spectra by fitting with six Gaussians is exemplified in Figure 3b. The main features of the spectra are as follows: (i) a relatively sharp Raman band peaking at ∼67 cm^{-1}, (ii) a broad band of lower amplitude with flat maxima at ∼96 cm^{-1}, and (iii) a band peaking at ∼153 cm^{-1}. The band peaking at ∼67 cm^{-1} is asymmetric due to the presence of two bands with maxima at ∼67 and ∼58 cm^{-1} (Figure 3b). The broad band covering the range of ∼80−130 cm^{-1} is composed of two bands peaking at ∼95 and ∼110 cm^{-1}. The Raman band with a maximum at ∼153 cm^{-1} has a small shoulder, which was fitted with a Gaussian band of low intensity peaking at ∼179 cm^{-1}.

Based on available literature data, bands with maxima at ∼67 and ∼153 cm^{-1} could be associated with A_{1g} and A_{3g} Raman-active modes, respectively.[38−40] Using the 785 nm excitation laser, it is observed that the band at 153 cm^{-1} has a higher intensity compared to the other main bands than the one with excitation at 532 nm. Similarly, Gong et al.[40] observed that the A_{3g}/A_{1g} intensity ratio is lower at 532 nm.

A plausible assignment of the ∼96 cm^{-1} broad band composed of two bands peaking at ∼110 and ∼95 cm^{-1} might be that it is coming from the overlap of A_{2g} and B_{3g} modes (identified at ∼130 and ∼108 cm^{-1} in SnSe single crystals[38]), whose frequencies are somewhat shifted due to the strongly preferential orientation of SnSe orthorhombic crystals as confirmed through XRD data. All mentioned A_g modes as well as the B_{3g} mode are rigid shear modes of a layer with respect to its adjacent layers; they determine the characteristic planar vibration modes of the SnSe orthorhombic structure.[38,41] It was also observed by Gong et al.[40] that when the PLD films were annealed, the two bands peaking at ∼110 and ∼95 cm^{-1} tended to shift to higher wavenumbers (127 and 104 cm^{-1}) and to be better resolved, which was associated with better crystallinity of the layers. The B_{1g} mode shows two Raman-active components (∼133 and 57 cm^{-1}) in SnSe single crystals.[38] The first component probably contributes to the Raman band with a maximum at 110 cm^{-1}. The second component may form a weak Raman band, which was fitted with a maximum at 58 cm^{-1}. Finally, the origin of the low-intensity band coming from the Raman spectra decomposition (∼179 cm^{-1}) is not clear and is not observed in the case of the 532 nm excitation.

One could speculate about the possible presence of tin oxides on the surface of the deposited PLD films. It cannot be

https://doi.org/10.1021/acsomega.1c01892
ACS Omega 2021, 6, 17483−17491

completely excluded; however, there is no evidence for common tin oxides, whose Raman-active vibrations are located at 112 and 210 cm^{-1} (E_g and A_{1g} modes of SnO)[42] or at 476, 638 and 782 cm^{-1} (E_g, A_{1g}, and B_{2g} modes of SnO_2).[43]

The thickness of the deposited samples under study, determined by ellipsometry, was in the range of ∼170−180 nm (Table 1). The values of surface roughness found by fitting of ellipsometry data are in the 3.5−4.3 nm range with a subtle maximum for thin films containing 0.5 atom % of As. These values are substantially larger than the values obtained by AFM (Figure 1). However, this discrepancy is in line with the fact that in ellipsometry, surface roughness is fitted using effective medium approximation, which includes both physical roughness and surface native oxides, which might be present. Moreover, the measurement spot is much larger in case of ellipsometry.[32]

The values of band gap estimated via the Cody−Lorentz (CL) model are between 0.90 and 0.96 eV (Table 1). Nevertheless, it is difficult to see any trend as the error bars are of the order of 0.04 eV. To see a comparison, bulk SnSe has an indirect band gap of ∼0.90 eV and a direct band gap of ∼1.30 eV.[44] Further, indirect band-gap values of SnSe nanosheets, nanoflowers, nanocolumns, and nanoplates were reported as 0.86, 0.95,[45] 0.93, and 0.96 eV,[46] respectively. The indirect band gap of vacuum-deposited polycrystalline thin films was reported to be 0.935[47] or 0.895 eV.[48] Thermally evaporated polycrystalline SnSe thin films exhibit a range of indirect band-gap values depending on the deposition rate (0.87−0.97 eV) and thickness (0.87−1.13 eV).[41] Laser-ablated thin films showed a direct band gap of 0.94 eV.[49] It can be concluded that the optical band-gap values obtained from the CL model for PLD $Sn_{50-x}As_xSe_{50}$ thin films are in very good agreement with already published results.

Urbach energy (E_u), which represents the width of the localized-states tail (present in the forbidden gap) typically associated with the amorphous state, was deducted from the CL model; the obtained values are given in Table 1. One can see that with increasing arsenic content in the $Sn_{50-x}As_xSe_{50}$ layers, the values of Urbach energy decrease, implying that the width of the localized-states tail is getting smaller. The E_u values reported in this work are coherent with those published for thermally evaporated SnSe thin films of comparable thickness (E_u ∼ 0.23 eV for ∼150 nm thick layers).[50]

Best-fit optical functions, i.e., refractive index and extinction coefficient spectral dependencies, deducted from spectroscopic ellipsometry data analysis for PLD $Sn_{50-x}As_xSe_{50}$ thin films are shown in Figure 4. As seen, in the studied spectral region, the refractive index and extinction coefficient vary drastically. Table 1 gives the refractive index values at two wavelengths, i.e., at 400 and 1550 nm. It is important to note that reported values indicate that the refractive index depends on the arsenic concentration in the layers. In detail, the films containing 0.5 atom % of As present the largest refractive index value at 400 nm and lowest value at 1550 nm. Regarding the refractive index, the data presented in this work are not well comparable with literature;[48,51] however, we believe that our values are reliable because of the good quality of the variable-angle spectroscopic ellipsometry data fitting, which is documented by the low values of mean square errors reaching 4.1 at maximum.

It is noteworthy to mention the extraordinary behavior of thin films with 0.5 atom % of As, which show the lowest crystallite size, maximum FWHM of XRD peaks, lowest unit

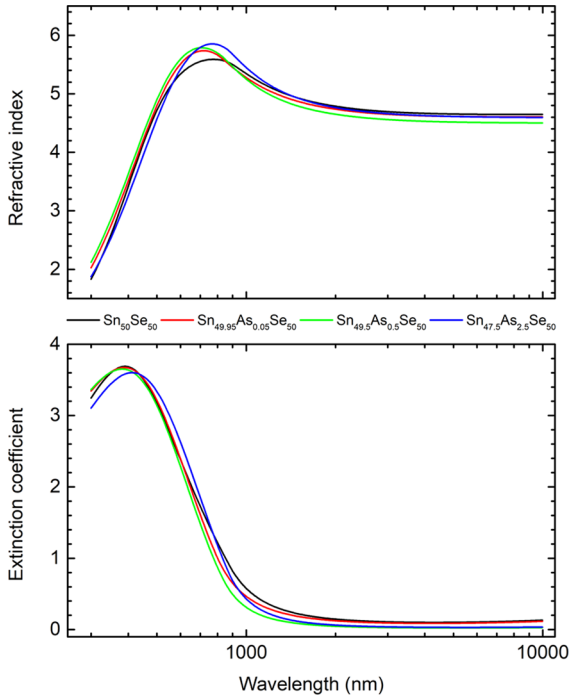

Figure 4. Optical functions of PLD $Sn_{50-x}As_xSe_{50}$ (x = 0, 0.05, 0.5 and 2.5) thin films: spectral dependencies of refractive indices (top) and extinction coefficients (bottom).

cell volume, as well as largest values of refractive index at 400 nm and lowest values at 1550 nm. These findings can be linked with the high concentration of Sn vacancies and divacancies.[24] A large number of vacancies is an important attribute of a "good" phase-change material.[25] Even if the films studied in this work are crystalline, we believe that further increase of the amount of vacancies might be possible, which may lead to the amorphous state. The fabrication of amorphous pure or doped Sn−Se thin films will be the focus of our next investigation exploiting a simple strategy of changing the basic stoichiometry from $Sn_{50}Se_{50}$ to compositions richer in selenium, keeping in mind the work of Chung.[19]

The clusters generated via laser ablation of $Sn_{50-x}As_xSe_{50}$ thin films and powders were studied by employing QIT-TOFMS. For the $Sn_{50-x}As_xSe_{50}$ powders, majority of the clusters were found in the mass-to-charge ratio (hereinafter m/z) range of 90−700. The mass spectra produced in the negative ion mode were of lower intensity in comparison with the positive mode. The effect of laser energy on the mass spectra intensities was thus studied in the positive mode (Figure 5).

The maximum intensities were found for a laser energy of 160 au. Apart from Sn_m^+, Se_n^+, and $Sn_mSe_n^+$ clusters (Table 2), several oxygen (hydrogen)-containing clusters were also detected, such as $Sn_xO_y^+$, $Sn_xO_yH_z^+$, $Se_xO_y^+$, and $Sn_xSe_yO_z^+$. Examples of selected mass spectra are given in Figure 6, where stoichiometries of the identified clusters are also provided. The oxygen-containing clusters may originate from a negligible oxide thin layer on the sample surface. Due to laser ablation of the sample surface, oxygen-containing species are detected. On the other hand, due to the small quantity of oxides, these are not detected via "bulk" methods like XRD or Raman scattering spectrometry.

In the case of $Sn_{50-x}As_xSe_{50}$ thin films, measurements were again more effective in positive ion mode, as the clusters

https://doi.org/10.1021/acsomega.1c01892
ACS Omega 2021, 6, 17483−17491

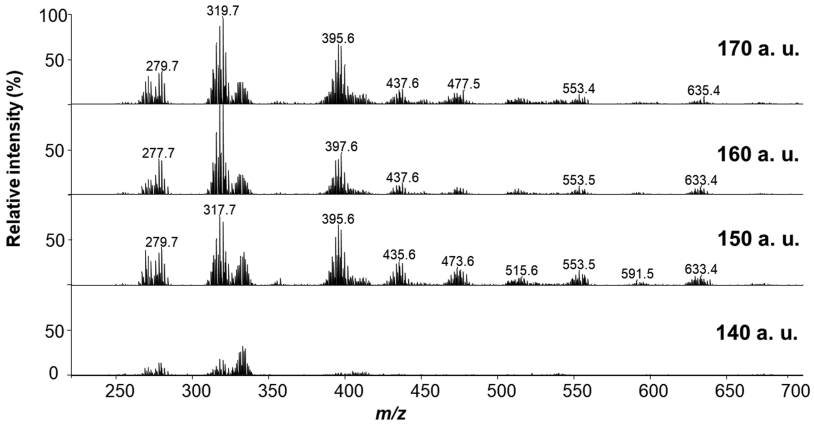

Figure 5. Effect of laser energy on the mass spectra intensities of $Sn_{50}Se_{50}$ powder sample (normalized to 19 mV).

Table 2. Clusters Identified in the Mass Spectra of $Sn_{50-x}As_xSe_{50}$ (x = 0, 0.05, 0.5, and 2.5) Powders[a]

x = 0	x = 0.05	x = 0.5	x = 2.5
Positive ion mode			
Se^+ Sn^+ Se_2^+ $SnSe^+$ Sn_2^+ Se_3^+ $SnSe_2^+$ Sn_2Se^+ Sn_3^+ $Sn_2Se_2^+$ Sn_3Se^+ Sn_4^+ Sn_5^+ $Sn_4Se_2^+$ Sn_5Se^+ Sn_6^+	Se^+ Sn^+ Se_2^+ $SnSe^+$ Sn_2^+ Se_3^+ $SnSe_2^+$ Sn_2Se^+ Sn_3^+ $Sn_2Se_2^+$ Sn_3Se^+ Sn_4^+ Sn_5^+	Se^+ Sn^+ Se_2^+ $SnSe^+$ Sn_2^+ Se_3^+ $SnSe_2^+$ Sn_2Se^+ Sn_3^+ $Sn_2Se_2^+$ Sn_3Se^+ Sn_4^+ Sn_5^+	Se^+ Sn^+ Se_2^+ $SnSe^+$ Sn_2^+ Se_3^+ $SnSe_2^+$ Sn_2Se^+ Sn_3^+ $Sn_2Se_2^+$ Sn_3Se^+ Sn_4^+ Sn_5^+
Negative ion mode			
Se^- Se_2^- Sn^- $SnSe^-$ $SnSe_2^-$	Se^- Se_2^- Sn^- $SnSe^-$ $SnSe_2^-$ Sn_2Se^-	Se^- Se_2^- Sn^- $SnSe^-$ $SnSe_2^-$	Se^- Se_2^- Sn^- $SnSe^-$ $SnSe_2^-$

[a]Gray color indicates low-intensity species.

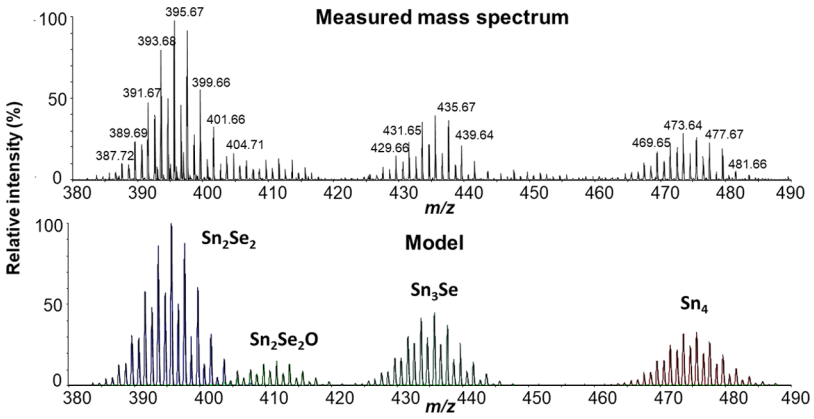

Figure 6. Example of the part of the measured mass spectrum of $Sn_{50}Se_{50}$ powder for a laser energy of 150 au and a model mass spectrum (for resolutions of 3500, 100× Sn_2Se_2, 15× Sn_2Se_2O, 50× Sn_3Se, 40× Sn_4).

produced in negative ion mode were of lower intensities. The clusters were formed in the m/z range of 90−350. The effect of laser energy on the mass spectra intensities was thus also studied in the positive ion mode (Figure 7). The maximum intensities were found for a laser energy of 170 au. Apart from Sn_m^+, low-intensity Se_n^+ and $Sn_mSe_n^+$ clusters (Table 3) and several oxygen (hydrogen)-containing clusters were also detected, especially $Sn_xO_y^+$, $Sn_xO_yH_z^+$, and $Sn_xSe_yO_z^+$. We note that in comparison with an earlier report,[49] the number of species identified in this work is higher, probably due to the better sensitivity/resolution of the exploited QIT-TOFMS system.

https://doi.org/10.1021/acsomega.1c01892
ACS Omega 2021, 6, 17483−17491

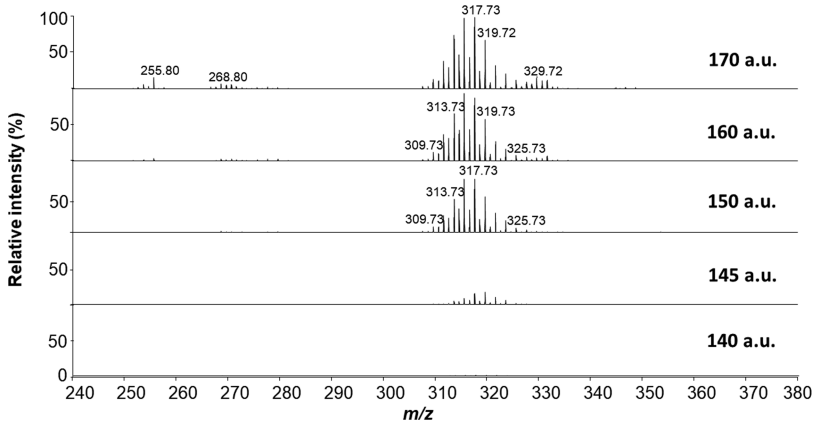

Figure 7. Effect of laser energy on the mass spectra intensities of a $Sn_{50}Se_{50}$ thin film (normalized to 43 mV).

Table 3. Clusters Identified in the Mass Spectra of $Sn_{50-x}As_xSe_{50}$ (x = 0, 0.05, 0.5, and 2.5) PLD Thin Films[a]

x = 0	x = 0.05	x = 0.5	x = 2.5
Positive ion mode			
Se^+ Sn^+ Se_2^+ $SnSe^+$ Sn_2^+ Se_3^+ $SnSe_2^+$ Sn_2Se^+ Se_4^+ $SnSe_3^+$ $Se_5^+/Sn_2Se_2^+$	Se^+ Sn^+ Se_2^+ $SnSe^+$ Sn_2^+ Se_3^+ $SnSe_2^+$ Se_4^+ $SnSe_3^+$ $Se_5^+/Sn_2Se_2^+$	Se^+ Sn^+ Se_2^+ $SnSe^+$ Sn_2^+ Se_3^+ $SnSe_2^+$ Se_4^+ $SnSe_3^+$ $Se_5^+/Sn_2Se_2^+$	Se^+ Sn^+ Se_2^+ $SnSe^+$ Sn_2^+ Se_3^+ $SnSe_2^+$ Se_4^+ $SnSe_3^+$ $Se_5^+/Sn_2Se_2^+$
Negative ion mode			
Se^- Se_2^- Sn^- $SnSe^-$ $SnSe_2^-$	Se^- Se_2^- Sn^- $SnSe^-$ $SnSe_2^-$ Sn_2Se^-	Se^- Se_2^- Sn^- $SnSe^-$ $SnSe_2^-$	Se^- Se_2^- Sn^- $SnSe^-$ $SnSe_2^-$

[a]Gray color indicates low-intensity species.

Clusters containing arsenic (oxygenated/hydrogenated) were identified in both $Sn_{50-x}As_xSe_{50}$ powders ($H_3As_2O^+$) and thin layers ($HAs_3O_6^+$ and $H_3As_3O_6^+$) due to differences between the measured mass spectra and model isotopic distributions. Signals of these clusters were unambiguously detectable only in the QIT-TOFMS spectra of samples with higher arsenic content.

To the best of our knowledge, the clusters in the Sn−Se system (and their structure) are known only for elements, i.e., tin[52−54] and selenium.[55−57] The structure of common SnSe is analogical to that of black phosphorus, where phosphorus atoms are replaced by Sn and Se atoms. The interlayer bonding in SnSe across the cleavage plane is between unlike atoms, i.e., Sn−Se. Adjacent layers are bound to each other with a combination of van der Waals and long-range electrostatic attractions.[3,44,58−60]

Probably due to alternation of the Sn and Se atoms in the SnSe structure, primarily peaks of $Sn_mSe_n^+$ clusters with low m and n values were identified in the mass spectra of both the $Sn_{50-x}As_xSe_{50}$ powders and thin films. On the other hand, the peaks related to clusters with high m or n values were of low intensity or absent. The main difference between the mass spectra of $Sn_{50-x}As_xSe_{50}$ powders and thin films was that peaks related to the clusters with m/z > 350 Da were not found in the mass spectra of the layers (Figures 5 and 7). However, analogical clusters were found in the mass spectra of the studied powders and thin films (Tables 2 and 3), differing in some cases in their relative intensities. In the case of thin films, the ablation threshold and optimum laser energy values were a bit higher in comparison with the powders.

3. CONCLUSIONS

Crystalline $Sn_{50-x}As_xSe_{50}$ (x = 0, 0.05, 0.5, and 2.5) thin films were fabricated from the corresponding hot-pressed targets via pulsed laser deposition. The chemical composition of the thin films is in good agreement with that of the targets. X-ray diffraction results showed that the films had been grown in a highly (h00) oriented orthorhombic SnSe phase. The films containing 0.5 atom % of As exhibited the lowest crystallite sizes, maximum FWHM of XRD peaks, and lowest unit cell volume. The temperature-dependent electrical resistance measurements showed a resistance drop of 3−4 orders of magnitude upon heating up to 400 °C. Raman scattering spectroscopy of the layers revealed A_{1g}, B_{3g}, A_{2g}, and A_{3g} modes. Band-gap values estimated by the analysis of spectroscopic ellipsometry data are within the range of 0.90−0.96 eV, being consistent with the data reported for SnSe thin films fabricated via other deposition techniques or nanosized SnSe. The refractive index spectral dependencies of PLD $Sn_{50-x}As_xSe_{50}$ thin films differ particularly from literature data, showing an extraordinary behavior for films doped with 0.5 atom % of As. The mass spectra of $Sn_{50-x}As_xSe_{50}$ thin films and parent powders were found to be similar: peaks of $Sn_mSe_n^+$ clusters with low m and n values predominate, while species

https://doi.org/10.1021/acsomega.1c01892
ACS Omega 2021, 6, 17483−17491

with high m or n values were of low intensity or absent. Some differences between the QIT-TOFMS spectra of thin films and powders were found in the ablation threshold, occurrence of high m/z peaks, and relative intensities of signals of certain clusters. Mass spectra signals related to oxygenated/hydrogenated tin/selenium species were also identified.

4. MATERIALS AND METHODS

4.1. Samples. Polycrystalline samples with the composition $Sn_{50-x}As_xSe_{50}$ (x = 0, 0.05, 0.5, and 2.5) were prepared by high-temperature reactions. Samples were synthesized from the stoichiometric mixtures of the 5 N elements (Sn and Se) and the compound (AsSn, synthesized). The AsSn compound was prepared by heating the stoichiometric mixture of Sn (5 N) and As (three times sublimed) at 933 K for 14 days in a vacuum-sealed (~10^{-3} Pa) quartz ampoule. Synthesis of the samples was done in evacuated quartz ampoules by heating the stoichiometric mixture (1.7 K/min) up to 1223 K. Ampoules were kept at this temperature for 6 h followed by free cooling to room temperature in the turned-off furnace.

The resulting bulk materials were powdered in agate mortar and hot-pressed at 713 K and 80 MPa for 1 h in a graphite die. The sample with the highest x was hot-pressed at a lower temperature (633 K) to keep suitable mechanical properties. Compact disc-shaped samples (with diameter 25 mm and thickness ~4 mm) reached 89−96% of the theoretical density. These discs were consequently used as targets for PLD.

$Sn_{50-x}As_xSe_{50}$ thin films were obtained via PLD. Chalcogenide targets were ablated with a KrF excimer laser emitting at 248 nm using 125 (±3) mJ output pulse energies, 30 ns pulse duration, and 20 Hz repetition rate. Laser energy density was set at ~2 J/cm^2. The thin films were deposited in a vacuum chamber (the pressure during deposition: $(5.7 \times 10^{-6})-(1.6 \times 10^{-5})$ Pa, background pressure: $4.2-(5 \times 10^{-6}$ Pa)). To obtain films with good thickness uniformity, the off-axis PLD technique exploiting rotating substrates and targets was used. Rotation speeds were ~5°/min for both targets and substrates. Pieces of single-crystalline ⟨100⟩ oriented silicon wafers (boron doped, p-type; thickness 0.525 mm; resistivity 75−95 Ω cm) and microscope glass slides (10 mm × 10 mm) were used as substrates; these were mounted parallel to the target surface at a distance of 6 cm. The temperature of the substrates was not controlled. The duration of the PLD process was chosen to fabricate thin films with a thickness of ~170−180 nm.

4.2. Instrumentation. The chemical compositions of the used targets and deposited layers were assessed by scanning electron microscopy linked with an energy-dispersive X-ray spectroscopy analyzer (SEM-EDS, JEOL JSM 6400). The morphology and topography of pulsed laser-deposited $Sn_{50-x}As_xSe_{50}$ films were analyzed by atomic force microscopy (AFM, Solver NEXT, NT-MDT). The tapping mode imaging was used (scanned area 2 μm × 2 μm). The SEM technique was also employed to observe the thin films' morphology using a field-emission gun SEM (JSM 6301F). The X-ray diffraction (XRD) technique was exploited to determine the structure of $Sn_{50-x}As_xSe_{50}$ layers using two instruments: D8-Advance diffractometer (Bruker AXS) and MiniFlex 600 (Rigaku). The XRD patterns were measured at room temperature from 5 to 90° (2θ) within 0.01 or 0.02° steps.

Raman scattering data of the films were recorded in backscattering geometry using a high-spectral-resolution (focal length 800 mm) LabRAM HR Evolution Raman spectrometer (HORIBA Scientific) coupled to a confocal microscope (objective 100×). For the excitation of Raman scattering spectra, a laser emitting at 785 nm was employed, with power of a few milliwatts to avoid the photosensitivity effect. The used grating had 600 grooves/mm.

The optical properties of the fabricated layers were investigated using two ellipsometers (VASE and IR VASE, J. A. Woollam Co.): the first ellipsometer had an automatic rotating analyzer for the spectral range 0.3−2.3 μm (UV−near-infrared (NIR)), measuring 100 revolutions with a resolution of 20 nm at selected angles of incidence (65, 70, and 75°); the second ellipsometer had a rotating compensator for the 1.7−10 μm range using angles of incidence as mentioned above, 20 scans, 15 spectra per revolution, and a resolution of 8 cm^{-1}. For the analysis of ellipsometry data in a broad, measured spectral region (0.3−10 μm), the Cody−Lorentz oscillator model was used.[61,62]

The measurements of temperature-dependent electrical resistance were carried out in the heating stage MHCS622E (Microptik) using a two-point method. The measurement was performed in a cell filled with Ar with the pressure slightly above the atmospheric pressure. The heating interval was set from room temperature to 400 °C with a heating rate of 2 °C/min.

Mass spectra were recorded in both positive and negative ion modes using the mass spectrometer AXIMA Resonance from Kratos Analytical Ltd. (Manchester, U.K.) coupled with a quadrupole ion trap and time-of-flight detection. This instrument was exploited for measurements from an m/z of ~90. For lower m/z values, AXIMA CFR (Kratos Analytical Ltd.) was employed. A reflectron mode was employed to record the mass spectra in both ion modes. The instruments were equipped with a nitrogen pulsed laser operating at a wavelength of 337 nm. The laser repetition rate was set to 5 Hz with a pulse time width of 3 ns. In both ion modes, the mass spectra were collected by accumulating the data from ~1000 laser pulses. The laser energy varied in arbitrary units (au) in the range of 0−180. Calibration of the mass spectrometer was made using red phosphorus,[63] which was purchased from Riedel de Haën (Hannover, Germany) and purified via sublimation in a nitrogen atmosphere before the usage. For mass spectrometry measurements, thin films on silicon substrates were fixed to the sample plate with an adhesive tape. The corresponding $Sn_{1-x}As_xSe$ powder samples were suspended in acetonitrile (1 mg/mL). From this suspension, 10 μL was deposited on a sample plate and dried.

4.3. Software and Computation. Stoichiometry of the detected clusters was determined via computer modelling of the isotopic envelopes using Launchpad software (Kompact version 2.9.3, 2011) from Kratos Analytical Ltd. (Manchester, U.K.). However, for low-intensity clusters, in negative mode especially, it was impossible to identify the clusters unambiguously, because of the similar molecular masses of Se_3 (236.88 Da) and Sn_2 (237.38 Da).

■ AUTHOR INFORMATION

Corresponding Author

Petr Němec − *Department of Graphic Arts and Photophysics, Faculty of Chemical Technology, University of Pardubice, 53210 Pardubice, Czech Republic;* orcid.org/0000-0003-2426-3078; Phone: +420466037247; Email: petr.nemec@upce.cz

https://doi.org/10.1021/acsomega.1c01892
ACS Omega 2021, 6, 17483−17491

Authors

Lubomír Prokeš − *Department of Chemistry, Faculty of Science, Masaryk University, 62500 Brno, Czech Republic*

Magdaléna Gorylová − *Department of Graphic Arts and Photophysics, Faculty of Chemical Technology, University of Pardubice, 53210 Pardubice, Czech Republic*

Kateřina Čermák Šraitrová − *Institute of Applied Physics and Mathematics, Faculty of Chemical Technology, University of Pardubice, 53210 Pardubice, Czech Republic*

Virginie Nazabal − *Univ Rennes, CNRS, ISCR UMR6226, ScanMAT UMS 2001, F-35000 Rennes, France; Department of Graphic Arts and Photophysics, Faculty of Chemical Technology, University of Pardubice, 53210 Pardubice, Czech Republic;* orcid.org/0000-0002-0113-3935

Josef Havel − *Department of Chemistry, Faculty of Science, Masaryk University, 62500 Brno, Czech Republic;* orcid.org/0000-0002-6675-5671

Complete contact information is available at: https://pubs.acs.org/10.1021/acsomega.1c01892

Notes

The authors declare no competing financial interest.

■ ACKNOWLEDGMENTS

This work was funded with support from the Czech Science Foundation (Project no. 19-24516S). The authors appreciate the financial support from the LM2018103 project funded by the Ministry of Education, Youth and Sports of the Czech Republic. The support from Platform Spectroscopy Infrared and Raman (SIR - ScanMAT, Université de Rennes 1) is acknowledged. Finally, the authors are thankful to Prof. Č. Drašar and Dr. K. Melánová for the fruitful discussions and XRD measurements, respectively.

■ REFERENCES

(1) Zhang, Z.; Zhao, X. X.; Li, J. SnSex flowerlike composites as anode materials for sodium ion batteries. *Mater. Lett.* **2016**, *162*, 169−172.

(2) Zhang, C. L.; Yin, H. H.; Han, M.; Dai, Z. H.; Pang, H.; Zheng, Y. L.; Lan, Y. Q.; Bao, J. C.; Zhu, J. M. Two-Dimensional Tin Selenide Nanostructures for Flexible All-Solid-State Supercapacitors. *ACS Nano* **2014**, *8*, 3761−3770.

(3) Shi, W. R.; Gao, M. X.; Wei, J. P.; Gao, J. F.; Fan, C. W.; Ashalley, E.; Li, H. D.; Wang, Z. M. Tin Selenide (SnSe): Growth, Properties, and Applications. *Adv. Sci.* **2018**, *5*, No. 1700602.

(4) Chen, Z. G.; Shi, X. L.; Zhao, L. D.; Zou, J. High-performance SnSe thermoelectric materials: Progress and future challenge. *Prog. Mater. Sci.* **2018**, *97*, 283−346.

(5) Protsak, I. S.; Champet, S.; Chiang, C. Y.; Zhou, W. Z.; Popuri, S. R.; Bos, J. W. G.; Misra, D. K.; Morozov, Y. M.; Gregory, D. H. Toward New Thermoelectrics: Tin Selenide/Modified Graphene Oxide Nanocomposites. *ACS Omega* **2019**, *4*, 6010−6019.

(6) Rehman, S. U.; Butt, F. K.; Hayat, F.; Ul Haq, B.; Tariq, Z.; Aleem, F.; Li, C. B. An insight into a novel cubic phase SnSe for prospective applications in optoelectronics and clean energy devices. *J. Alloys Compd.* **2018**, *733*, 22−32.

(7) Feleni, U.; Ajayi, R.; Jijana, A.; Sidwaba, U.; Douman, S.; Baker, P.; Iwuoha, E. Tin Selenide Quantum Dots Electrochemical Biotransducer for the Determination of Indinavir - A Protease Inhibitor Anti-Retroviral Drug. *J. Nano Res.* **2017**, *45*, 12−24.

(8) Zhao, L. D.; Lo, S. H.; Zhang, Y. S.; Sun, H.; Tan, G. J.; Uher, C.; Wolverton, C.; Dravid, V. P.; Kanatzidis, M. G. Ultralow thermal conductivity and high thermoelectric figure of merit in SnSe crystals. *Nature* **2014**, *508*, 373−377.

(9) Wei, P. C.; Bhattacharya, S.; He, J.; Neeleshwar, S.; Podila, R.; Chen, Y. Y.; Rao, A. M. The intrinsic thermal conductivity of SnSe. *Nature* **2016**, *539*, E1−E2.

(10) Feutelais, Y.; Majid, M.; Legendre, B.; Fries, S. G. Phase diagram investigation and proposition of a thermodynamic evaluation of the tin-selenium system. *J. Phase Equilib.* **1996**, *17*, 40−49.

(11) Okamoto, H. Se-Sn (selenium-tin). *J. Phase Equilib.* **1998**, *19*, 293.

(12) Nguyen-Cong, K.; Gonzalez, J. M.; Steele, B. A.; Oleynik, I. I. Tin-Selenium Compounds at Ambient and High Pressures. *J. Phys. Chem. C* **2018**, *122*, 18274−18281.

(13) Mukhokosi, E. P.; Krupanidhi, S. B.; Nanda, K. K. Band Gap Engineering of Hexagonal SnSe2 Nanostructured Thin Films for Infra-Red Photodetection. *Sci. Rep.* **2017**, *7*, No. 15215.

(14) Li, X. Y.; Li, L.; Zhao, H. C.; Ruan, S. C.; Zhang, W. F.; Yan, P. G.; Sun, Z. H.; Liang, H. W.; Tao, K. Y. SnSe2 Quantum Dots: Facile Fabrication and Application in Highly Responsive UV-Detectors. *Nanomaterials* **2019**, *9*, No. 1324.

(15) Tan, P. F.; Chen, X.; Wu, L. D.; Shang, Y. Y.; Liu, W. W.; Pan, J.; Xiong, X. Hierarchical flower-like SnSe2 supported Ag3PO4 nanoparticles: Towards visible light driven photocatalyst with enhanced performance. *Appl. Catal., B* **2017**, *202*, 326−334.

(16) Liu, M.; Shi, Y.; Zhang, G. P.; Zhang, Y. H.; Wu, M. M.; Ren, J. F.; Man, B. Y. Surface-Enhanced Raman Spectroscopy of Two-Dimensional Tin Diselenide Nanoplates. *Appl. Spectrosc.* **2018**, *72*, 1613−1620.

(17) Moreira, Ó. L. C.; Cheng, W. Y.; Fuh, H. R.; Chien, W. C.; Yang, W. J.; Fei, H. F.; Xu, H. J.; Zhang, D.; Chen, Y. H.; Zhao, Y. F.; Lv, Y. H.; Wu, G.; Lv, C. Z.; Arora, S. K.; Coileain, C. O.; Heng, C. L.; Chang, C. R.; Wu, H. C. High Selectivity Gas Sensing and Charge Transfer of SnSe2. *ACS Sens.* **2019**, *4*, 2546−2552.

(18) Veeralingam, S.; Sahatiya, P.; Badhulika, S. Low cost, flexible and disposable SnSe2 based photoresponsive ammonia sensor for detection of ammonia in urine samples. *Sens. Actuators, B* **2019**, *297*, No. 126725.

(19) Chung, K. M.; Wamwangi, D.; Woda, M.; Wuttig, M.; Bensch, W. Investigation of SnSe, $SnSe_2$, and Sn_2Se_3 alloys for phase change memory applications. *J. Appl. Phys.* **2008**, *103*, No. 083523.

(20) Chen, C. L.; Wang, H.; Chen, Y. Y.; Day, T.; Snyder, G. J. Thermoelectric properties of p-type polycrystalline SnSe doped with Ag. *J. Mater. Chem. A* **2014**, *2*, 11171−11176.

(21) Li, J. C.; Li, D.; Qin, X. Y.; Zhang, J. Enhanced thermoelectric performance of p-type SnSe doped with Zn. *Scr. Mater.* **2017**, *126*, 6−10.

(22) Gao, J. L.; Xu, G. Y. Thermoelectric performance of polycrystalline Sn1-xCuxSe (x=0-0.03) prepared by high pressure method. *Intermetallics* **2017**, *89*, 40−45.

(23) Duong, A. T.; Nguyen, V. Q.; Duvjir, G.; Duong, V. T.; Kwon, S.; Song, J. Y.; Lee, J. K.; Lee, J. E.; Park, S.; Min, T.; Lee, J.; Kim, J.; Cho, S. Achieving ZT=2.2 with Bi-doped n-type SnSe single crystals. *Nat. Commun.* **2016**, *7*, No. 13713.

(24) Sraitrova, K. C.; Cizek, J.; Holy, V.; Kasparova, J.; Plechacek, T.; Kucek, V.; Navratil, J.; Krejcova, A.; Drasar, C. As-doped SnSe single crystals: Ambivalent doping and interaction with intrinsic defects. *Phys. Rev. B* **2021**, *103*, No. 085203.

(25) Raoux, S.; Welnic, W.; Ielmini, D. Phase change materials and their application to nonvolatile memories. *Chem. Rev.* **2010**, *110*, 240−267.

(26) Song, L. R.; Zhang, J. W.; Iversen, B. B. Enhanced thermoelectric properties of SnSe thin films grown by single-target magnetron sputtering. *J. Mater. Chem. A* **2019**, *7*, 17981−17986.

(27) Chandra, G. H.; Kumar, J. N.; Rao, N. M.; Uthanna, S. Preparation and characterization of flash evaporated tin selenide thin films. *J. Cryst. Growth* **2007**, *306*, 68−74.

(28) Martínez-Escobar, D.; Ramachandran, M.; Sanchez-Juarez, A.; Rios, J. S. N. Optical and electrical properties of SnSe2 and SnSe thin films prepared by spray pyrolysis. *Thin Solid Films* **2013**, *535*, 390−393.

(29) Drozd, V. E.; Nikiforova, I. O.; Bogevolnov, V. B.; Yafyasov, A. M.; Filatova, E. O.; Papazoglou, D. ALD synthesis of SnSe layers and nanostructures. *J. Phys. D: Appl. Phys.* **2009**, *42*, No. 125306.
(30) Suen, C. H.; Shi, D. L.; Su, Y.; Zhang, Z.; Chan, C. H.; Tang, X. D.; Li, Y.; Lam, K. H.; Chen, X. X.; Huang, B. L.; Zhou, X. Y.; Dai, J. Y. Enhanced thermoelectric properties of SnSe thin films grown by pulsed laser glancing-angle deposition. *J. Materiomics* **2017**, *3*, 293−298.
(31) Němec, P.; Takats, V.; Csik, A.; Kokenyesi, S. GeSe/GeS nanomultilayers prepared by pulsed laser deposition. *J. Non-Cryst. Solids* **2008**, *354*, 5421−5424.
(32) Bouška, M.; Pechev, S.; Simon, Q.; Boidin, R.; Nazabal, V.; Gutwirth, J.; Baudet, E.; Nemec, P. Pulsed laser deposited GeTe-rich GeTe-Sb_2Te_3 thin films. *Sci. Rep.* **2016**, *6*, No. 26552.
(33) Cappelli, E.; Bellucci, A.; Medici, L.; Mezzi, A.; Kaciulis, S.; Fumagalli, F.; Di Fonzo, F.; Trucchi, D. M. Nano-crystalline Ag-PbTe thermoelectric thin films by a multi-target PLD system. *Appl. Surf. Sci.* **2015**, *336*, 283−289.
(34) Pangavhane, S. D.; Nemec, P.; Nazabal, V.; Moreac, A.; Jovari, P.; Havel, J. Laser desorption ionization time-of-flight mass spectrometry of erbium-doped Ga-Ge-Sb-S glasses. *Rapid Commun. Mass Spectrom.* **2014**, *28*, 1221−1232.
(35) Mawale, R. M.; Ausekar, M. V.; Prokes, L.; Nazabal, V.; Baudet, E.; Halenkovic, T.; Bouska, M.; Alberti, M.; Nemec, P.; Havel, J. Laser Desorption Ionization of As(2)Ch(3) (Ch = S, Se, and Te) Chalcogenides Using Quadrupole Ion Trap Time-of-Flight Mass Spectrometry: A Comparative Study. *J. Am. Soc. Mass Spectrom.* **2017**, *28*, 2569−2579.
(36) Mawale, R.; Halenkovic, T.; Bouska, M.; Gutwirth, J.; Nazabal, V.; Bora, P. L.; Pecinka, L.; Prokes, L.; Havel, J.; Nemec, P. Mass spectrometric investigation of amorphous Ga-Sb-Se thin films. *Sci. Rep.* **2019**, *9*, No. 10213.
(37) Šútorová, K.; Prokes, L.; Nazabal, V.; Bouska, M.; Havel, J.; Nemec, P. Laser Desorption Ionisation Time-of-Flight Mass Spectrometry of Chalcogenide Glasses from $(GeSe_2)_{100-x}(Sb_2Se_3)_x$ System. *J. Am. Ceram. Soc.* **2015**, *98*, 4107−4110.
(38) Chandrasekhar, H. R.; Humphreys, R. G.; Zwick, U.; Cardona, M. IR and Raman spectra of the IV-VI compounds SnS and SnSe. *Phys. Rev. B* **1977**, *15*, 2177−2183.
(39) Li, X. Z.; Xia, J.; Wang, L.; Gu, Y. Y.; Cheng, H. Q.; Meng, X. M. Layered SnSe nano-plates with excellent in-plane anisotropic properties of Raman spectrum and photo-response. *Nanoscale* **2017**, *9*, 14558−14564.
(40) Gong, X. N.; Feng, M. L.; Wu, H.; Zhou, H. P.; Suen, C. H.; Zou, H. J.; Guo, L. J.; Zhou, K.; Chen, S. J.; Dai, J. Y.; Wang, G. Y.; Zhou, X. Y. Highly (100)-orientated SnSe thin films deposited by pulsed-laser deposition. *Appl. Surf. Sci.* **2021**, *535*, No. 147694.
(41) Li, Z.; Guo, Y.; Zhao, F.; Nie, C.; Li, H.; Shi, J.; Liu, X.; Jiang, J.; Zuo, S. Effect of film thickness and evaporation rate on co-evaporated SnSe thin films for photovoltaic applications. *RSC Adv.* **2020**, *10*, 16749−16755.
(42) Luo, H.; Liang, L. Y.; Cao, H. T.; Liu, Z. M.; Zhuge, F. Structural, Chemical, Optical, and Electrical Evolution of SnO_x Films Deposited by Reactive rf Magnetron Sputtering. *ACS Appl. Mater. Interfaces* **2012**, *4*, 5673−5677.
(43) Geurts, J.; Rau, S.; Richter, W.; Schmitte, F. J. SnO films and their oxidation to SnO_2 - Raman scattering, IR reflectivity and X-ray diffraction studies. *Thin Solid Films* **1984**, *121*, 217−225.
(44) Lefebvre, I.; Szymanski, M. A.; Olivier-Fourcade, J.; Jumas, J. C. Electronic structure of tin monochalcogenides from SnO to SnTe. *Phys. Rev. B* **1998**, *58*, 1896−1906.
(45) Li, L.; Chen, Z.; Hu, Y.; Wang, X. W.; Zhang, T.; Chen, W.; Wang, Q. B. Single-Layer Single-Crystalline SnSe Nanosheets. *J. Am. Chem. Soc.* **2013**, *135*, 1213−1216.
(46) Jang, K.; Lee, I. Y.; Xu, J.; Choi, J.; Jin, J.; Park, J. H.; Kim, H. J.; Kim, G. H.; Son, S. U. Colloidal Synthesis of SnSe Nanocolumns through Tin Precursor Chemistry and Their Optoelectrical Properties. *Cryst. Growth Des.* **2012**, *12*, 3388−3391.
(47) Bhatt, V. P.; Gireesan, K.; Desai, C. F. Electrooptic properties of polycrystalline SnSe thin-films. *Cryst. Res. Technol.* **1989**, *24*, 187−192.
(48) Soliman, H. S.; Hady, D. A. A.; Rahman, K. F. A.; Youssef, S. B.; Elshazly, A. A. Optical properties of tin-selenid films. *Phys. A* **1995**, *216*, 77−84.
(49) Teghil, R.; Santagata, A.; Marotta, V.; Orlando, S.; Pizzella, G.; Giardiniguidoni, A.; Mele, A. Characterization of the plasma plume and of thin-film epitaxially produced during laser-ablation of SnSe. *Appl. Surf. Sci.* **1995**, *90*, 505−514.
(50) Kumar, N.; Parihar, U.; Kumar, R.; Patel, K. J.; Panchal, C. J.; Padha, N. Effect of film thickness on optical properties of tin selenide thin films prepared by thermal evaporation for photovoltaic applications. *Am. J. Mater. Sci.* **2012**, *2*, 41−45.
(51) El-Menyawy, E. M.; Azab, A. A.; El-Khalawany, L. M.; Okasha, N.; Terra, F. S. Influence of annealing temperatures on the structural, optical and electrical properties of SnSe films. *J. Mater. Sci.-Mater. Electron.* **2018**, *29*, 8354−8363.
(52) Majumder, C.; Kumar, V.; Mizuseki, H.; Kawazoe, Y. Small clusters of tin: Atomic structures, energetics, and fragmentation behavior. *Phys. Rev. B* **2001**, *64*, No. 233405.
(53) Oger, E.; Kelting, R.; Weis, P.; Lechtken, A.; Schooss, D.; Crawford, N. R. M.; Ahlrichs, R.; Kappes, M. M. Small tin cluster anions: Transition from quasispherical to prolate structures. *J. Chem. Phys.* **2009**, *130*, No. 124305.
(54) Drebov, N.; Oger, E.; Rapps, T.; Kelting, R.; Schooss, D.; Weis, P.; Kappes, M. M.; Ahlrichs, R. Structures of tin cluster cations Sn-3(+) to Sn-15(+). *J. Chem. Phys.* **2010**, *133*, No. 224302.
(55) Hohl, D.; Jones, R. O.; Car, R.; Parrinello, M. The structure of selenium clusters - Se_3 to Se8. *Chem. Phys. Lett.* **1987**, *139*, 540−545.
(56) Xu, W. G.; Bai, W. J. The selenium clusters Se-n (n=1-5) and their anions: Structures and electron affinities. *J. Mol. Struct.: THEOCHEM* **2008**, *854*, 89−105.
(57) Alparone, A. Density functional theory Raman spectra of cyclic selenium clusters Se-n (n=5-12). *Comput. Theor. Chem.* **2012**, *988*, 81−85.
(58) Taniguchi, M.; Johnson, R. L.; Ghijsen, J.; Cardona, M. Core excitons and conduction-band structures in orthorhombic GeS, GeSe, SnS, and SnSe single-crystals. *Phys. Rev. B* **1990**, *42*, 3634−3643.
(59) Kim, S. U.; Duong, A. T.; Cho, S.; Rhim, S. H.; Kim, J. A microscopic study investigating the structure of SnSe surfaces. *Surf. Sci.* **2016**, *651*, 5−9.
(60) Nguyen, V. Q.; Kim, J.; Cho, S. A Review of SnSe: Growth and Thermoelectric Properties. *J. Korean Phys. Soc.* **2018**, *72*, 841−857.
(61) Ferlauto, A. S.; Ferreira, G. M.; Pearce, J. M.; Wronski, C. R.; Collins, R. W.; Deng, X. M.; Ganguly, G. Analytical model for the optical functions of amorphous semiconductors from the near-infrared to ultraviolet: Applications in thin film photovoltaics. *J. Appl. Phys.* **2002**, *92*, 2424−2436.
(62) Baudet, E.; Sergent, M.; Nemec, P.; Cardinaud, C.; Rinnert, E.; Michel, K.; Jouany, L.; Bureau, B.; Nazabal, V. Experimental design approach for deposition optimization of RF sputtered chalcogenide thin films devoted to environmental optical sensors. *Sci. Rep.* **2017**, *7*, No. 3500.
(63) Kolářová, L.; Prokes, L.; Kucera, L.; Hampl, A.; Pena-Mendez, E.; Vanhara, P.; Havel, J. Clusters of Monoisotopic Elements for Calibration in (TOF) Mass Spectrometry. *J. Am. Soc. Mass Spectrom.* **2017**, *28*, 419−427.

https://doi.org/10.1021/acsomega.1c01892
ACS Omega 2021, 6, 17483−17491